

Experiments to investigate lift production mechanisms on pitching flat plates

P. R. R. J. Stevens¹  · H. Babinsky¹

Received: 9 June 2016 / Revised: 26 November 2016 / Accepted: 29 November 2016 / Published online: 29 December 2016
© The Author(s) 2016. This article is published with open access at Springerlink.com

Abstract Pitching flat plates are a useful simplification of flapping wings, and their study can provide useful insights into unsteady force generation. Non-circulatory and circulatory lift producing mechanisms for low Reynolds number pitching flat plates are investigated. A series of experiments are designed to measure forces and study the unsteady flowfield development. Two pitch axis positions are investigated, namely a leading edge and a mid-chord pitch axis. A novel PIV approach using twin laser lightsheets is shown to be effective at acquiring full field of view velocity data when an opaque wing model is used. Leading-edge vortex (LEV) circulations are extracted from velocity field data, using a Lamb–Oseen vortex fitting algorithm. LEV and trailing-edge vortex positions are also extracted. It is shown that the circulation of the LEV, as determined from PIV data, approximately matches the general trend of an unmodified Wagner function for a leading edge pitch axis and a modified Wagner function for a mid-chord pitch axis. Comparison of experimentally measured lift correlates well with the prediction of a reduced-order model for a LE pitch axis.

1 Introduction

The recent rise of micro-air vehicles (MAVs) has been profound. These miniature fliers have a wide range of revolutionary applications including, but not limited to, real-time data delivery surveillance (Davis et al. 1996) and

exo-planetary exploration (Young et al. 2000). MAVs can use flapping wing designs to take advantage of unsteady effects at low Reynolds numbers (Petricca et al. 2011). Flapping wing-style MAV designs could be improved with a better understanding of the governing physics of flapping wing motions. For example, more efficient flapping movements could provide longer battery life and hence increase flight duration. Of particular interest in the generation of an efficient motion is the fluid mechanical process by which lift is generated.

One approach for understanding unsteady lift generation is to study simplified flapping motions. The simplest case experimentally is that of a purely translating wing. Dickinson and Götz (1993) used the relative motion of an accelerated wing in a stationary fluid to analyse the Wagner effect (see Sect. 1.3) at Reynolds numbers relevant to insect/MAV flight. They also discussed the inertial, ‘*virtual mass*’ effect which occurred during transients.¹ Further work by Beckwith and Babinsky (2009) demonstrated that for small incidences, after the initial transient passes, Wagner’s theoretical prediction converges with the measured force data. Later, PittFord (2013) demonstrated how the leading-edge vortex (LEV) circulation on a high incidence surging wing could be reasonably well modelled using Wagner’s theorem and coupled with virtual mass to predict lift. It is not obvious that Wagner’s theorem should apply at all since it is for thin aerofoils at small incidence and attached flow. Thus, here we want to investigate further the idea that Wagner

✉ P. R. R. J. Stevens
robbie.stevens@cantab.net

¹ Department of Engineering, University of Cambridge, Trumpington Street, Cambridge CB2 1PZ, UK

¹ The non-circulatory effect occurs in an unsteady flow, i.e. when a wing is accelerated, a mass of fluid is accelerated with the wing, creating an inertial reaction force, which can contribute to the lift. There is no circulation associated with the production of this force. The effect is commonly called ‘*virtual mass*’.

might apply to a LEV (as opposed to bound circulation) for pitching flat plates at high incidence.

Another kinematic case that has received attention in the literature is that of a pitching wing in a constant freestream velocity (Ol 2009; Granlund et al. 2010; Wang and Eldredge 2012; Kang et al. 2013; Hartloper et al. 2013). Brunton and Rowley (2009) demonstrated that for attached flows, a simple model such as that of Theodorsen (1934), which includes both non-circulatory and circulatory effects can predict lift for a pure pitch motion reasonably well. Despite the great insight from these studies, there is still a lack of knowledge of the explicit fundamental lift producing mechanisms. The contribution of non-circulatory or circulatory mechanisms, which contribute to the lift force for high incidence pitch motions with separated flowfields, is one area that requires further study.

1.1 Virtual mass

The virtual mass problem for an accelerating flat plate at incidence is considered by Katz and Plotkin (2001) who explain that a pressure difference between the windward and rearward sides occurs creating a force. This force can be expressed as:

$$F = \frac{\rho c^2 \pi}{4} \dot{V} \quad (1)$$

where c is the wing chord and V is the plate normal velocity at the mid-chord as defined in Fig. 1.

For a pitching wing motion, the non-circulatory force is dependent upon the axis of pitch rotation. A simple flat-plate wing pitching about its mid-chord with no freestream for example should theoretically produce a net

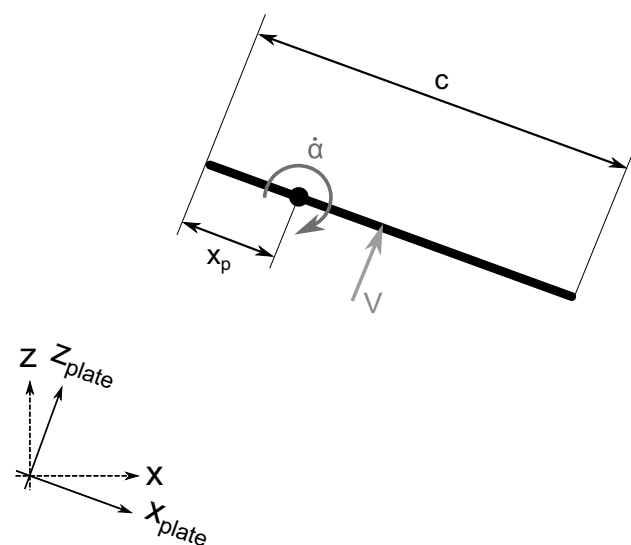


Fig. 1 Definition of pitch axis position

zero non-circulatory force since the upward and downward momentums imparted to different parts of the flow during the motion are equal. Contrastingly, a flat plate that pitches about an axis other than the mid-chord (such as the leading edge) should experience a noticeable non-circulatory force contribution.

1.2 Circulatory force: vortex lift

The classic way to interpret the concept of circulatory lift is via the *Kutta–Joukowski* theorem:

$$L' = \rho U_{\infty} \Gamma \quad (2)$$

where ρ is density, U_{∞} is freestream velocity and Γ is circulation. The *Kutta–Joukowski* relation holds true for simple aerofoils at small incidence in a steady flow. The flows of interest here, however, are unsteady, with an aerofoil at high incidence. A common feature of such separated flows is the formation of leading-edge vortex (LEV) and trailing-edge vortex (TEV) pairs. LEVs are in general not attached, typically advecting downstream relative to the aerofoil. Additionally, LEVs change strength. Under these two circumstances and in the context of Eq. 2, it is not therefore immediately obvious how the LEV contributes to lift.

PittFord (2013) established that for rapidly accelerating high incidence flat plates with a separated flow, the bound circulation tends towards zero and the circulatory component may be considered wholly contained within the LEV. This approximation was confirmed experimentally by PittFord and Babinsky (2014) for a translating, surging flat plate and by Percin and van Oudheusden (2015) for a revolving, surging flat plate.

Lamb (1932) defines a vortex pair of equal and opposite strength according to Fig. 2 and expresses the force imparted in the fluid as an impulse momentum according to:

$$\mathbf{J} = \rho \Gamma s \hat{\mathbf{e}}_n \quad (3)$$

where s is the distance between vortex centres and $\hat{\mathbf{e}}_n$ is a unit normal in a direction, which bisects a line joining the vortex pair at right angles. The impulse, \mathbf{J} may be decomposed into horizontal \mathbf{P} and vertical \mathbf{Q} components:

$$\mathbf{J} = \mathbf{P} + i\mathbf{Q} = \rho \Gamma [(z_{TEV} - z_{LEV}) + i(x_{LEV} - x_{TEV})] \quad (4)$$

Kármán and Sears (1938) explain that the rate of change of vertical momentum and thus the time derivative of the vertical impulse is equivalent to the lift force. Applying the chain rule to the complex part of Eq. 4 gives the lift force as:

$$L' = -\rho [(u_{LEV} - u_{TEV})\Gamma + (x_{LEV} - x_{TEV})\dot{\Gamma}] \quad (5)$$

PittFord (2013) demonstrates how this can be used to describe an expression for lift which has two vortex-related

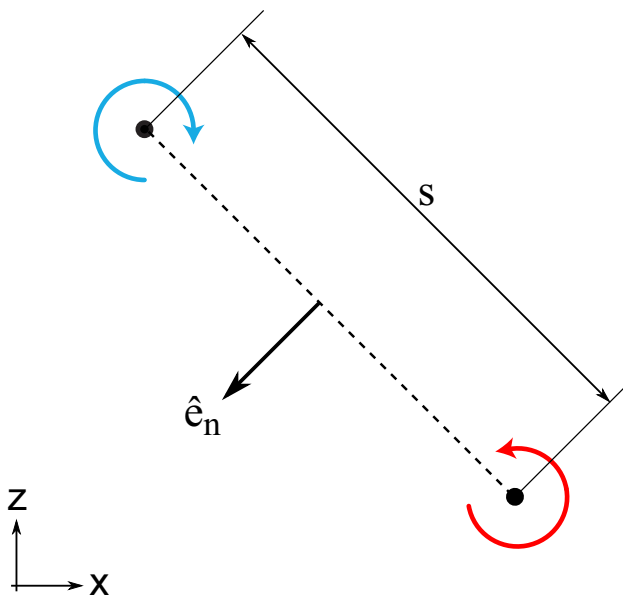


Fig. 2 Lamb's vortex pair

contributing components, namely one component related to the vortex strength and the relative movement between them and one related to the growth of circulation. These two components are referred to here as a vortex advection term (C_{LVA}) and a vortex growth term (C_{LVG}):

$$C_{LVA} = - \frac{2}{U_\infty^2 c} [(u_{LEV} - u_{TEV}) \Gamma_{LEV}] \tag{6}$$

$$C_{LVG} = - \frac{2}{U_\infty^2 c} [(x_{LEV} - x_{TEV}) \dot{\Gamma}_{LEV}] \tag{7}$$

These contributions form one way to understand the vortex lift for simple flapping motions. In order to use these equations to predict the circulatory lift component, the required dependencies are thus the LEV position, the LEV relative velocity and the circulation of the LEV. Babinsky et al. (2016) used this formulation to demonstrate that it is possible to make a reasonable prediction for lift if approximate values are used for vortex advection ($-(u_{LEV} - u_{TEV}) \approx 0.5U_\infty$) and a circulation based on a modified Wagner theorem. They also explained that for the vortex separation ($-(x_{LEV} - x_{TEV})$), a reasonable prediction for lift can be made by substituting the vortex separation with the chord length, c , under the assumption that when LEV circulation changes, vorticity is shed at the TE, which is approximately 1chord away. They also noted that for high incidences the chord length vortex separation should be adjusted to $c \cdot \cos\alpha$.

In order to test the model of Babinsky et al. (2016) and develop a better understanding of the physics, more information on vortex strengths and trajectories for

different types of motions (e.g. variation in pitch axis) is needed.

1.3 Circulatory force: circulation prediction

To obtain a theoretical circulation prediction, consider first the classical case of an impulsively started wing as shown in Fig. 3. Even for an impulsively started wing with attached flow, there is a lag in the attainment of the steady state value of bound circulation. Classically this effect has been modelled following the method of Wagner (1925). An impulsively started aerofoil sheds vorticity at the trailing edge forming a starting vortex (see Fig. 3). This vortex creates a downwash, which reduces the effective incidence and in turn inhibits the bound circulation. As the aerofoil moves away from the starting vortex, the effect diminishes and bound circulation grows. A reproduction of Wagner's original circulation and lift prediction is shown in Fig. 4. Graham (1983) extended Wagner's concept, explaining that the development of lift for an aerofoil undergoing a sudden change in motion is strongly dependent on the rate at which the effective incidence changes. This implies that for a constant streamwise velocity it might be possible to have a modified version of Wagner's prediction for a rotating wing (see Sect. 4.7).

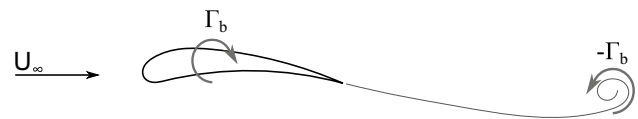


Fig. 3 Starting vortex and bound circulation

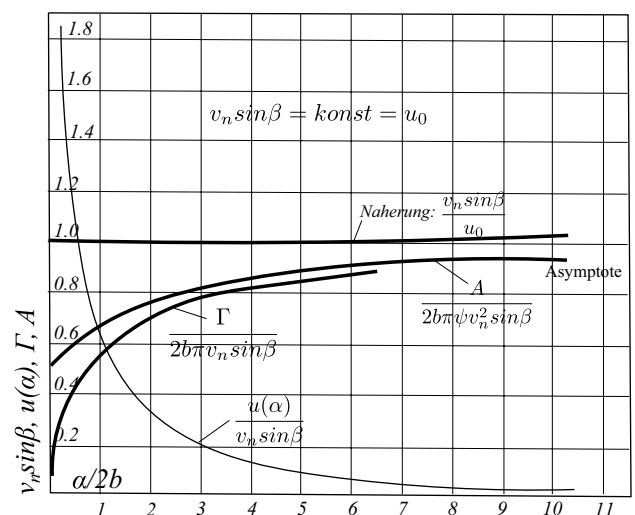


Fig. 4 Reproduction of original circulation and lift distributions predicted by Wagner (1925)

In Fig. 4, there is a difference between the Wagner calculation of circulation and the lift, which is most obvious at $t = 0$, where $\Gamma = 0$ but lift is finite. Despite circulation starting from zero, the time derivative of circulation has a finite value at $t = 0$. The bound circulation is the integral of vorticity along the plate, and it may be considered as having a physical position on the plate (typically the centre of gravity of the plate and not at the TE), which leads to a separation distance between the bound circulation and the starting vortex and thus there will be a lift contribution even at $t = 0$, according to Eq. 8.

1.4 Kinematic lift: ‘Magnus lift’

A direct theoretical prediction of the lift additionally requires a lift contribution due to rotation for a pitching wing. This lift contribution was previously been discussed by Babinsky et al. (2016) and may be considered akin to the Magnus effect. Following a similar approach to the virtual camber formulation for a pitching wing (Leishman 2000; Babinsky et al. 2016) represented this term as:

$$C_{LMG} = \frac{\pi c}{2U_\infty} \cdot \dot{\alpha} \quad (8)$$

where $\dot{\alpha}$ is the first derivative of the pitch angle. This term is due to the kinematic rotation and is henceforth referred to as the ‘Magnus’ term. The Magnus term is directly equivalent to the second Fourier harmonic for quasi-steady aerofoil theory.

1.5 Aim and approach

The aims of this paper are fourfold. The first is to acquire LEV topology, strength and trajectory data for a wider range of kinematics than has already been reported in the literature. Secondly, the LEV strength data are compared with Wagner’s classic model. The third aim is to explore modifications to Wagner’s model that might better represent specific kinematic cases. Finally, a comparison is made between the reduced-order model of Babinsky et al. (2016) and experimental data for both a LE and mid-chord pitch axis.

The experimental configuration is a simple flat plate undergoing a combined translation and pitch motion. Two configurations are investigated, namely one with a rotation axis at the LE and one at the mid-chord. Planar particle image velocimetry (PIV) is used to acquire flowfield data. A Lamb–Oseen vortex fitting algorithm is applied to determine a noise-reduced calculation of LEV circulation from the PIV data.

The simple wing geometry and motion is chosen to facilitate experiments, however, may be considered as a gross simplification of a real MAV/insect-style wing. A

finite \mathcal{R} wing ($\mathcal{R} = 4$) is selected for this study. This \mathcal{R} gives a reasonably 2D flowfield across most of the span, with tip vortex effects being confined to the near-tip region. The tip effects may influence forces; however, one goal of this work is to demonstrate that 2D-based theory could be used to give a reasonable approximation of the lift forces of moderate \mathcal{R} MAV/insect-style wings.

An item of uncertainty for a mid-chord pitch axis is whether there are any vortical structures on the lower surface created by the shear layer separating from the LE beneath the plate, as the plate pitches up. When an opaque wing is used with PIV there is typically a shadow region (zone of no information), thus to establish the complete flowfield for this case, a novel twin-lightsheet PIV method is developed.

2 Experimental set-up

Experiments are conducted at the Cambridge University Engineering Department water towing tank facility. A schematic of the facility is shown in Fig. 5. The tank has a length of 7 m, width of 1 m and a 2-m long working section, which has clear side walls and floor for optical access. The operational cross section is 0.8 m². The facility has a computer controlled, motor-driven carriage.

For this work, the carriage is translated at a constant speed to give a chord based Reynolds number of 10,000. A maximum error of $\approx 2.5\%$ in Reynolds number is achieved by adjustment of the carriage velocity with temperature within the bounds defined by Fig. 6, which are defined based on (White’s 2011) curve fits for variations in density and viscosity. The Reynolds number error corresponds to approximately a ± 1 °C variation in water temperature. The \mathcal{R} , wing is manufactured from carbon fibre and has a rounded LE shape, has chord(c) of 0.12 m and has a thickness of 2.5%.

2.1 Pitch kinematics

A schematic of the pitching wing mechanism is shown in Fig. 7. PIV and dye flow visualisation are conducted at

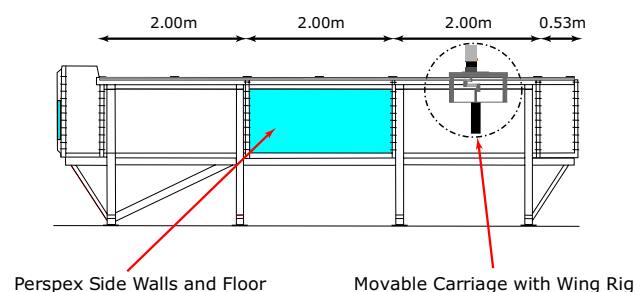


Fig. 5 Tow tank facility schematic

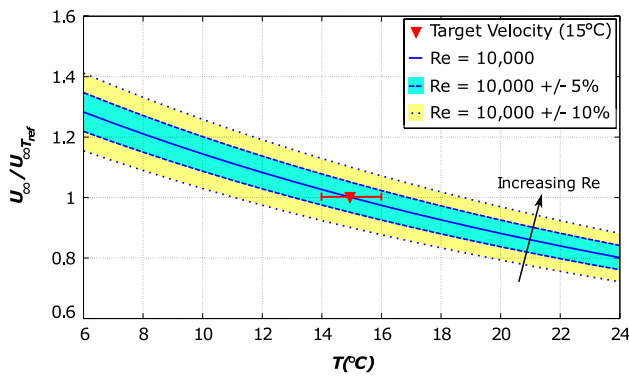


Fig. 6 Velocity range required to achieve $Re = 10,000$ based on variations in density and viscosity with temperature

2c from the free tip (mid-span) of the wing. A skim plate removes any influence of free-surface effects and acts as a symmetry plane for the wing, giving an effective \mathcal{R} of twice the physical \mathcal{R} . Pitch rotation is achieved using a stepper motor and is triggered by an optical switch mounted on the side of the tank.

In the experiments described here, a fast pitch rate of reduced frequency, $k = 0.392$ is analysed ($k = \dot{\alpha}c/2U_\infty$, where $\dot{\alpha}$ is the pitch rate $d\alpha/dt$ with α describing the incidence of the wing). The pitch rate is chosen to be equivalent to a rotation occurring over a translation distance of $1c$ when the wing is translating at $Re = 10,000$. The pitch is combined with a translation of the wing. The wing moves in translation at $\alpha = 0^\circ$ and $Re = 10,000$. The pitching motion is then triggered with the maximum geometric pitch angle set to $\alpha = 45^\circ$. The method of Wang and Eldredge (2012) is used to determine the smoothing

of the pitch ramp profile, giving a smoothing parameter value of $a_s = 11$.

2.2 Force measurements

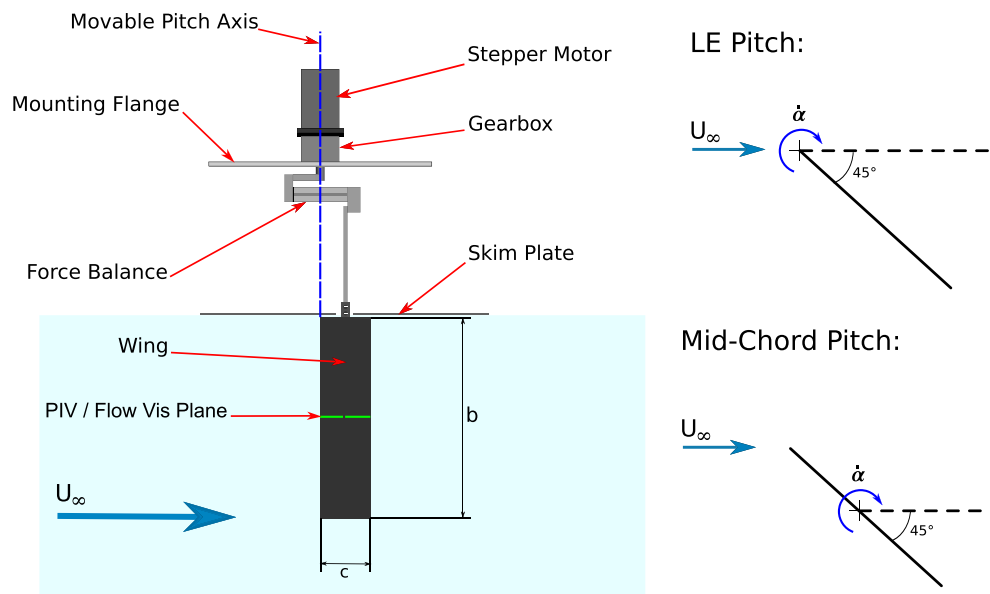
A *Flow Dynamics*, two-component balance, is used. Forces are acquired at 1 kHz. The balance is mounted such that forces are measured normal and tangential to the plate at zero incidence. The measured forces are thus resolved into the lift and drag directions. Only lift is reported in this paper. The balance is calibrated using known masses. Data are averaged over 10 runs, reducing the standard error of the mean by $1/\sqrt{10}$ (Peters 2001), and a moving point average of 100 data points is used to smooth the data, with the ends treated with progressively fewer data points.

To extract the fluid mechanical forces, it is necessary to remove inertial effects from the measured signal. To find the inertial effect of the wing, the same motion kinematics are performed in air and it is assumed that the data acquired is representative of the inertial force exerted since the aerodynamic forces in air are negligible compared to water.

2.3 Planar PIV

The *LA Vision* high-speed PIV system comprises a *Litron LDY304* Nd:YLF laser and a pair of *Phantom M310* high-speed CMOS cameras which have a resolution of 1280×800 pixels and maximum frame rate capability of 3260 Hz at full resolution. The cameras are fitted with 50 mm lenses. The seeding is titanium dioxide (TiO_2). In standard configuration, the system is used with a single camera and lightsheet. The laser sheet thickness is approximately 1 mm, when focussed at the mid-plane of the Field Of View

Fig. 7 Wing pitching mechanism and pitch axis definition



(FOV). This configuration produces a shadow region with an opaque model. The standard arrangement is modified for the mid-chord pitch axis case to take complete flowfield measurements by employing a twin laser lightsheet and the second camera.

Vector fields are processed with *LA Vision's DaVis V.8* software, using a cross-correlation on sequential images. The calculation is conducted with two passes of interrogation window size 32×32 pixels, followed by two passes of interrogation window size 16×16 pixels. A 50% interrogation window overlap is used.

2.4 Twin laser sheet planar PIV

The general optical arrangement for the twin laser sheet setup is shown in Fig. 8. The arrangement uses two cameras for the purpose of providing unobscured data on both sides of the opaque wing model and does not give 'out-of-plane' velocities. The output from the laser is passed through a beam splitter. *Beam 1* is passed through the optical guiding arm to the *sheet 1*-forming optics. *Beam 2* passes under the tow tank and is directed to the *sheet 2*-forming optics. The high-speed cameras do not block the beam path under the tank. Care is taken to ensure that light from the beam is not incident on the camera lens. When the source beam is split, the light intensity

of each resultant beam is approximately halved. The power of the source beam is therefore adjusted accordingly to ensure that a suitable light intensity is achieved for PIV images.

The sheet-forming optics are in line and create a laser sheet overlap. The approximate thickness of both laser sheets is approximately 1 mm when focussed at the mid-plane of the FOV. This overlap is illustrated from a top view in Fig. 9 and creates a fully illuminated flowfield in the vicinity of the opaque wing.

A maximum flatness deviation of 1 mm over the calibrated plane corresponds to an angle of 0.1° (Fig. 10). With both the beams crossing over at the mid-position, then the maximum misalignment at the edge of a typical FOV (300 mm) is 0.25 mm.

2.4.1 Comment on PIV error

The PIV error may be simplistically represented by:

$$\Sigma \epsilon_{PIV} = \epsilon_{bias} + \epsilon_{rms_0} + \epsilon_{rms_s} + \epsilon_{rms_\rho} + \epsilon_{rms_i} \quad (9)$$

The contributions include, uncertainty due to loss of particle images pairs due to out-of-plane motion (ϵ_{bias}), particle image diameter (ϵ_{rms_0}), particle image displacement (ϵ_{rms_s}), interrogation window particle density (ϵ_{rms_ρ}) and variations in particle image intensities (ϵ_{rms_i}). The errors in terms of

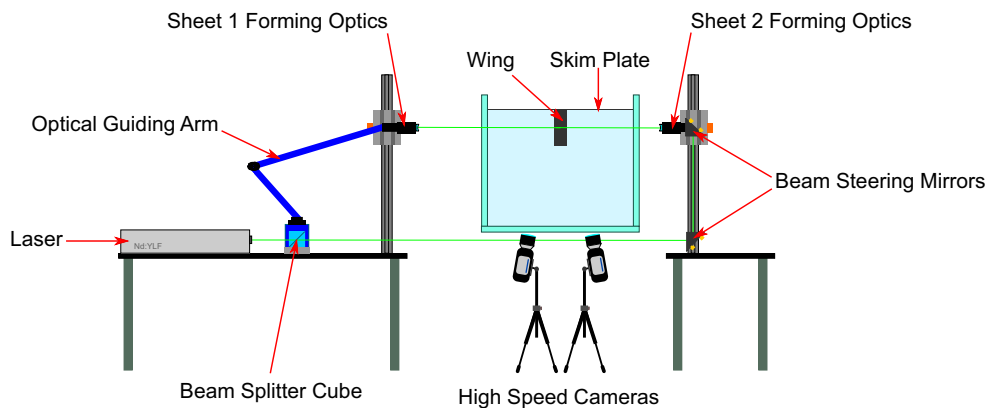
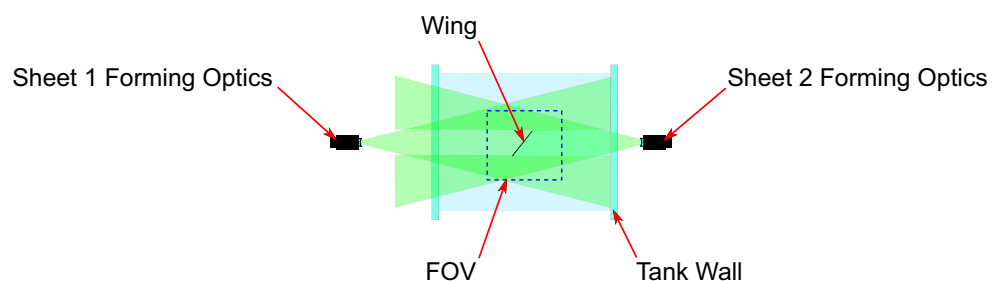


Fig. 8 General optical arrangement for twin laser sheet planar PIV

Fig. 9 Top view of twin laser sheet planar PIV overlap



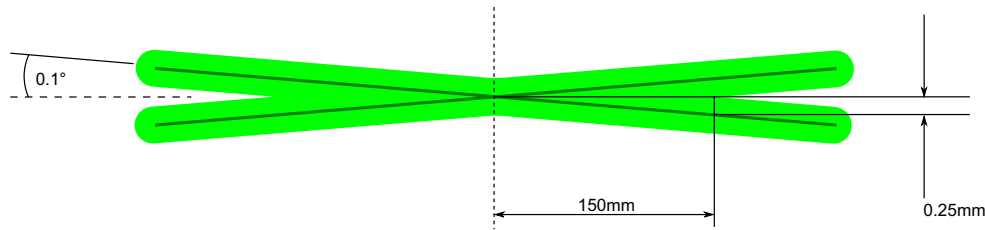


Fig. 10 Laser Sheet overlap Alignment. Note that beam angles are exaggerated for clarity

Table 1 Summary of PIV errors

Error source	Pixel error
ϵ_{bias}	-0.01
ϵ_{rms_0}	0.01
ϵ_{rms_s}	0.01
ϵ_{rms_p}	0.025
ϵ_{rms_t}	0.1
$\Sigma \epsilon_{PIV}$	0.135

image pixels are summarised in Table 1. The errors are estimated based principally on the methods of Raffel et al. (2007), with the exception of the particle image intensity, which is based on the method of Nobach and Bodenschatz (2009). The total error $\Sigma \epsilon_{PIV} = 0.135$ pixels is equivalent to a 2.7% error in freestream velocity.²

2.5 Flow visualisation

Flow visualisation is performed using a dye composed of milk and water. Milk is used as it improves the stability of dye filaments, retarding diffusion of the filament into the main bulk of the fluid; milk also has the advantage of possessing good reflective properties (Clayton and Massey 1967). The chordwise injection position is at $0.2c$ and the spanwise position is at c from the free wing tip.

To aid with interpretation of flow topology, PIV streamlines are superimposed onto flow visualisation images. The streamlines are shown in the frame of reference moving with the wing. The wing speed is added during processing since the PIV system is stationary.

The flow visualisation technique creates a *streakline*, where fluid elements are connected by a line, which passed through a single point. In a steady flow, streamlines and streaklines are identical. In an unsteady flow, however, the patterns produced will vary, i.e the dye path history shown by the dye flow image will generally not be the same as the instantaneous streamline

² This assumes a pixel shift between frames of 5 pixels.

pattern. Comparing the two directly can be informative in unsteady flows.

3 Data reduction

3.1 Circulation calculation

The circulation of the LEV is computed by a Lamb–Oseen best fit method applied to the experimental data.

Morgan et al. (2009) investigated several approaches for calculation of the circulation of vortices in planar PIV data. To mitigate some error when a vortex core is insufficiently resolved, Morgan et al. (2009) identified that computing circulation around circular contours, emanating from a known vortex centre, is one possible approach. This work uses such an approach combined with a Lamb–Oseen best fit.

First, the vortex is located using the γ_2 -criterion method of Graftieaux et al. (2001), then the axis of rotation for the vortex is determined. The axis is found by calculating the centroid of multiple γ_2 contours ($0.4 < \gamma_2 < 0.8$) and averaging. Using the axis of rotation as an epicentre, the circulation around multiple circular contours of increasing radius is calculated. The circulation for each contour is found according to:

$$\Gamma = \oint_{c_r} \mathbf{u} \cdot d\mathbf{l} \tag{10}$$

where c_r is the contour at any given radius, r . This generates a series of circulation values emanating from the vortex epicentre.

To fit a theoretical distribution to the computed circulation data, a Lamb–Oseen vortex with circulation described by:

$$\Gamma = \Gamma_0 \left(1 - \exp\left(\frac{-r^2}{r_c^2(t)}\right) \right) \tag{11}$$

is used. The unknown coefficients Γ_0 and r_c are varied automatically until a least squares fit to the radial computed circulation distribution is achieved. Figure 11a shows the

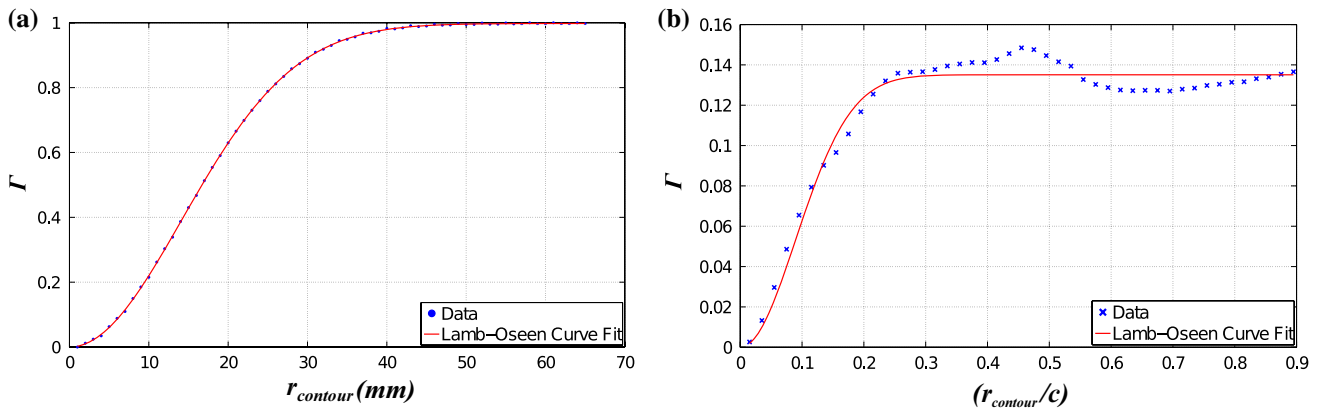


Fig. 11 Lamb–Oseen radial Γ fits **a** Synthetic vortex Lamb–Oseen fit, $\Gamma_{max} = 1$. **b** LEV Lamb–Oseen fit, $\alpha = 45^\circ$, $Re = 10,000$

Lamb–Oseen best fit to calculated radial circulation data points for a synthetic vortex with $r_c = 20$ mm, $\Gamma = 1$ and 20% noise added to the theoretical velocity data. The fit R^2 is almost 100%. For the real example of a pitching wing LEV in Fig. 11b, the R^2 is 96%.

In Fig. 11b, for the region $0.3 < r_{contour}/c < 0.8$, the Lamb–Oseen vortex circulation does not quite fit that of the real data. There is an overshoot in circulation followed by an undershoot. There are a number of possible causes for this behaviour. One possibility is that a Lamb–Oseen vortex is assumed to be laminar and according to Govindaraju and Saffman (1971), an overshoot in circulation suggests that the real vortex may in fact be turbulent. In reality if an overshoot occurs, it is probably caused by a non-axisymmetric instability which is difficult to model. Also, the flows under investigation do not involve simple vortices, with features such as the wing plate in the vicinity of vortices, which may affect the velocity field. One possible reason that there is an undershoot in circulation with increasing radius may be because the LEV is adjacent to the plate, where opposite-sign vorticity may be generated on the surface (see Panah et al. 2014

for example), which is being included in the circulation circuit. In this work, the curve fitting procedure assumes that the LEV velocity field is close to a Lamb–Oseen vortex. The consequence of this assumption is that if an LEV becomes turbulent, the calculated circulation may be greater. It will be seen how this has important ramifications.

4 Results and discussion

4.1 Wind off forces

The ‘wind off’ lift histories for a LE and a mid-chord pitch axis, respectively, are shown in Fig. 12. These cases have $U_\infty = 0$ and a reduced frequency of $k = \infty$. The angular rate, $\dot{\alpha}$, is thus used to describe the pitch rate. The x -axes of Fig. 12 are labelled s/c which corresponds to time, non-dimensionalised by the length of the pitch period. The lift coefficient is defined here by non-dimensionalising the ‘wind off’ lift force by the ‘wind on’ dynamic pressure experienced at $Re = 10,000$.

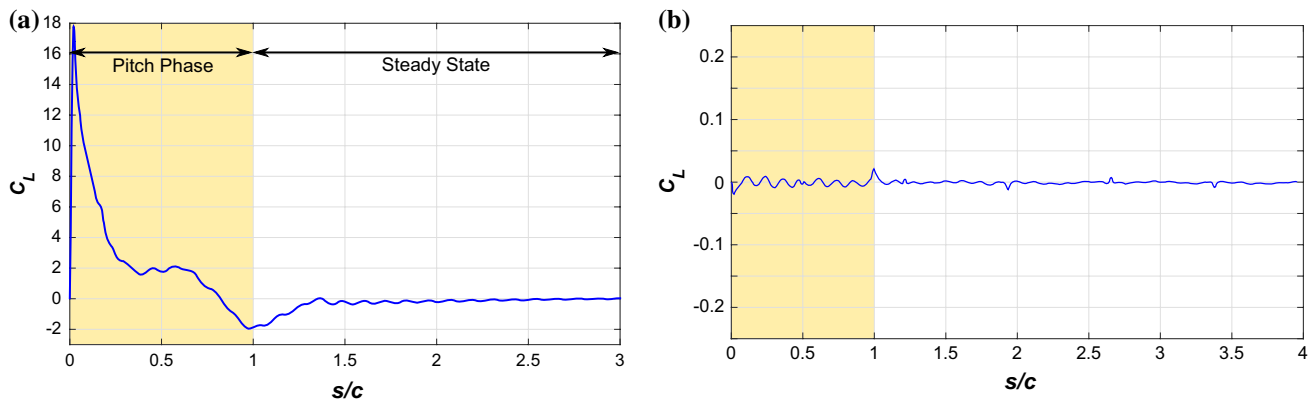


Fig. 12 Wind off lift coefficient variation with pitch axis for $\dot{\alpha} = 0.523 \text{ rad s}^{-1}$, $k = \infty$ ($U_\infty = 0$). **a** LE pitch axis. **b** Mid-chord pitch axis

For the LE pitch axis case of Fig. 12a, a large non-circulatory spike occurs at the initiation of pitch rotation. This is followed by a sharp drop and a levelling off at a C_L of approximately 2 by $s/c \approx 0.5$. There is a further drop starting at $s/c \approx 0.7$, with a minimum³ reached at $s/c \approx 1$. The lift coefficient is approximately 0 by $s/c \approx 1.5$. The small fluctuations which remain are attributed to residual wing vibration.⁴

The mid-chord pitch axis case of Fig. 12b shows the measured force is approaching the noise floor. This confirms that the mass of fluid accelerated by the upper and lower wing surfaces is equal from symmetry. There is a small fluctuation in lift that has a sinusoidal form. This is again attributed to rig vibration. It is recognised that for a mid-chord pitch axis with a freestream, there is a possibility of a nonzero, non-circulatory force; however, it is expected that ‘wind on’ forces are dominated by circulatory effects.

4.2 Wind on forces

It has already been seen in the previous section that shifting the pitch axis can have a profound effect on the lift force history. The most prominent difference is the apparent absence of non-circulatory effects when pitching about the mid-chord. The comparison of the ‘wind on’ lift histories for the respective pitch axes is made in Fig. 13, with the pitching region enlarged in Fig. 14 for clarity. Considering both figures in tandem and first focussing on the LE pitch axis lift history (blue curve), there is an initial spike in lift coefficient at the start of the pitch motion. A sharp drop and a second rise to a value of just above 5 follows. Subsequently there is another sharp drop and a further rise to a value of approximately 2.2. Following the end of pitching, there is a prominent feature, where the lift coefficient achieves a value of approximately 2.8. Thereafter the lift coefficient slowly tends towards a value in the region of 0.7–0.8. This occurs after $s/c \approx 15$. There is a small, lift maximum around $s/c = 8$.

For the mid-chord pitch axis lift history (green curve), it is observed that during pitching, there is a rise in lift, peaking at a C_L just above 4. This is followed by a sharp drop.

³ It is noted that the downward non-circulatory spike, which occurs at the end of pitching should have a magnitude, which is equal to the product of the magnitude of the initial spike at the start of pitching and the cosine of the maximum incidence angle ($\cos 45^\circ$). The magnitude of the negative spike in the force history is not as large as expected considering non-circulatory forces in isolation and perhaps other effects, such as the presence of vortices are influencing the measured C_L in this region.

⁴ The frequency of vibration aligns approximately with the natural frequency of the rig as determined by comparison of the FFT from a strike test.

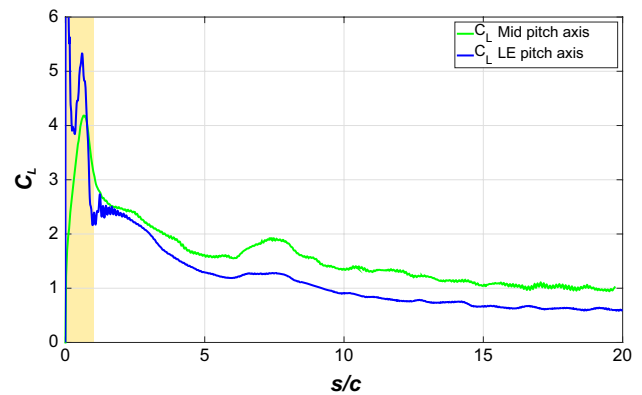


Fig. 13 Wind on lift force axis variation comparison

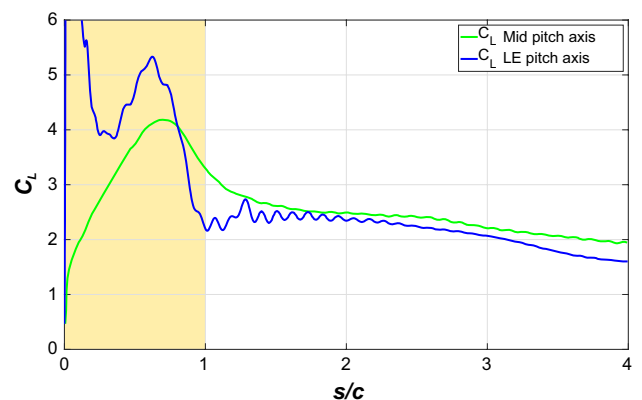


Fig. 14 Wind on lift force axis variation comparison pitching region detail

The rate of drop off in lift slows after pitching has ended. A secondary maximum in the lift coefficient occurs around $s/c = 7$. The lift then continues to fall until $s/c = 15$, at which point the flow is considered to have reached a steady state condition with a C_L of approximately 1.⁵

There is a notable difference in the final ‘steady state’ lift coefficient values, with the mid-chord pitch axis value being approximately 30% greater than the LE pitch axis at $s/c = 15$. This result is outside the error margin in steady state velocity and was found to be repeatable. It is expected that over very long advective timescales, the ‘steady state’ lift coefficient values will converge; however, this could not be tested due to the physical limitation of the length of the towing tank facility. Nevertheless, it is clear that the

⁵ In the absence of measurements for values of $s/c > 20$, there is some uncertainty over the absolute value of the steady state. For the purposes of discussion here, a steady state is assumed when there is no significant change in trend expected thereafter.

ultimate steady state value takes a long time to become independent of the initial kinematics ($s/c > 15$).

4.3 Flow topology

Figures 15 and 16 show streamlines superimposed on top of dye flow images for a LE and a mid-chord pitch axis, respectively, with the pitching part of the motion in the left-hand column and the fixed incidence translation in the right hand column of each figure.

4.4 LE pitch axis flow topology

Consider first, the pitch part of the motion for the LE pitch axis case in the left-hand column of Fig. 15. Shortly after pitch has started at $s/c = 0.167$, the flow appears to be almost attached everywhere on the plate. Streamline curvature indicates the initiation of a growth in lift. By $s/c = 0.5$, the starting vortex creates a kink in the streamlines. This is slightly out of phase with the starting vortex visualised from the dye injection and might be expected considering the difference between a streakline and streamline in an unsteady flow. This illustrates the problems of relying on flow visualisations in unsteady flows. A small LEV is now also visible. At $s/c = 0.833$, the LEV has grown in size and the flow appears to still be attached over the rear portion of the plate. By $s/c = 1$, the LEV has grown and is starting to exhibit advection. Furthermore, the streamlines are no longer attached over the aft portion of the plate.

During the translation part of the motion, at $s/c = 2$ there is still high streamline curvature above the wing. The LEV is visualised as having grown in diameter and the dye is dispersing, indicating a loss of coherence. By $s/c = 3$, the LEV has lost any visible coherency and the flow over the flat plate is considered stalled. At $s/c = 5$, the flow is still stalled. At $s/c = 8$, it is noticed that there is a distinct change in the flow topology. Above the aerofoil, the dye is more concentrated and the streamlines show an increase in curvature, which has the appearance of a pseudo-reattachment of the flow to the TE. This pseudo-reattachment when taken in consideration with the force history of Fig. 13 seems to correlate with the small lift maximum which occurs around $s/c = 8$.

4.5 Mid-chord pitch axis flow topology

The mid-chord pitch axis case presented here takes advantage of the double lightsheet method to provide complete flowfield information. The mid-chord pitch axis case of Fig. 16 shows similarly attached streamlines to those seen for the LE pitch axis case at $s/c = 0.167$. Again by $s/c = 0.5$, the starting vortex has created a kink in the streamlines near the TE. A very clear LEV is visible and again the streamline curvature has increased; however, in contrast

to the LE pitch axis case, it appears that the streamlines do not remain attached to the aft part of the plate. It is, however, recognised that the streamline attachment may have a dependence on the choice of streamlines. By $s/c = 0.833$, a clear LEV is now visible. At $s/c = 1$, the LEV has grown; however, it has not noticeably advected aft from the LE.

During the translation part of the motion, at $s/c = 2$, the LEV has started to advect aft away from the LE. By $s/c = 3$, the streamlines show noticeable divergence with some streamlines reversing. This reversal combined with the dissipation of dye from the flow visualisation suggests that the lift may be dropping. Also notice that some streamlines appear to 'stop' in the flow. This phenomenon is likely linked to out-of-plane fluid motion. At $s/c = 5$, the dye has dispersed further and there is an increase in streamline divergence. At $s/c = 8$, the dye and streamlines are bending towards the TE once more, indicating that the lift may slightly increase.

4.6 Vortex dynamics

LEV position relative to the LE is defined according to Fig. 17. The TEV position relative to the TE is similarly defined. The trajectories of the LEV and TEVs are given in Fig. 18.

4.6.1 LE pitch axis vortex dynamics

The LEV trajectory is seen in Fig. 18a. While pitching, the LEV has an almost constant position relative to the plate ($r_{LEV} \approx 0.1$). At the end of pitch, the LEV starts to advect away from the LE at a much higher rate than during the pitching phase, until the end of the detectable range ($s/c \approx 1.2$ in this case).

The plot of Fig. 18b shows two distinct TEVs. The first TEV is tracked until the formation of a second, at which point it is tracked. *TEV 1* shows a linear growth in x position. *TEV 2* also shows a linear growth but with a downward drift of the core position in y .

When moving away from the wing, it appears that both the LEV and TEV do so at a constant speed (within the available observation time). A crude estimate of the advection velocities is obtained by fitting a straight line. While the wing is pitching, the LEV advects at $u_{LEV} \approx 0.1U_\infty$. The TEVs advect at the same rate, with $u_{TEV1} \approx 0.6U_\infty$ and $u_{TEV2} \approx 0.6U_\infty$, respectively. In this case, the first TEV is considered to have the dominant influence while pitching. This is a crude estimation. The relative advection velocity will then have a magnitude of approximately $0.5U_\infty$.

4.6.2 Mid-chord pitch axis vortex dynamics

For the mid-chord pitch axis case, while pitching, the LEV trajectory (Fig. 18c) remains at an almost constant x position of ≈ 0.1 relative to the LE. This suggests an attached

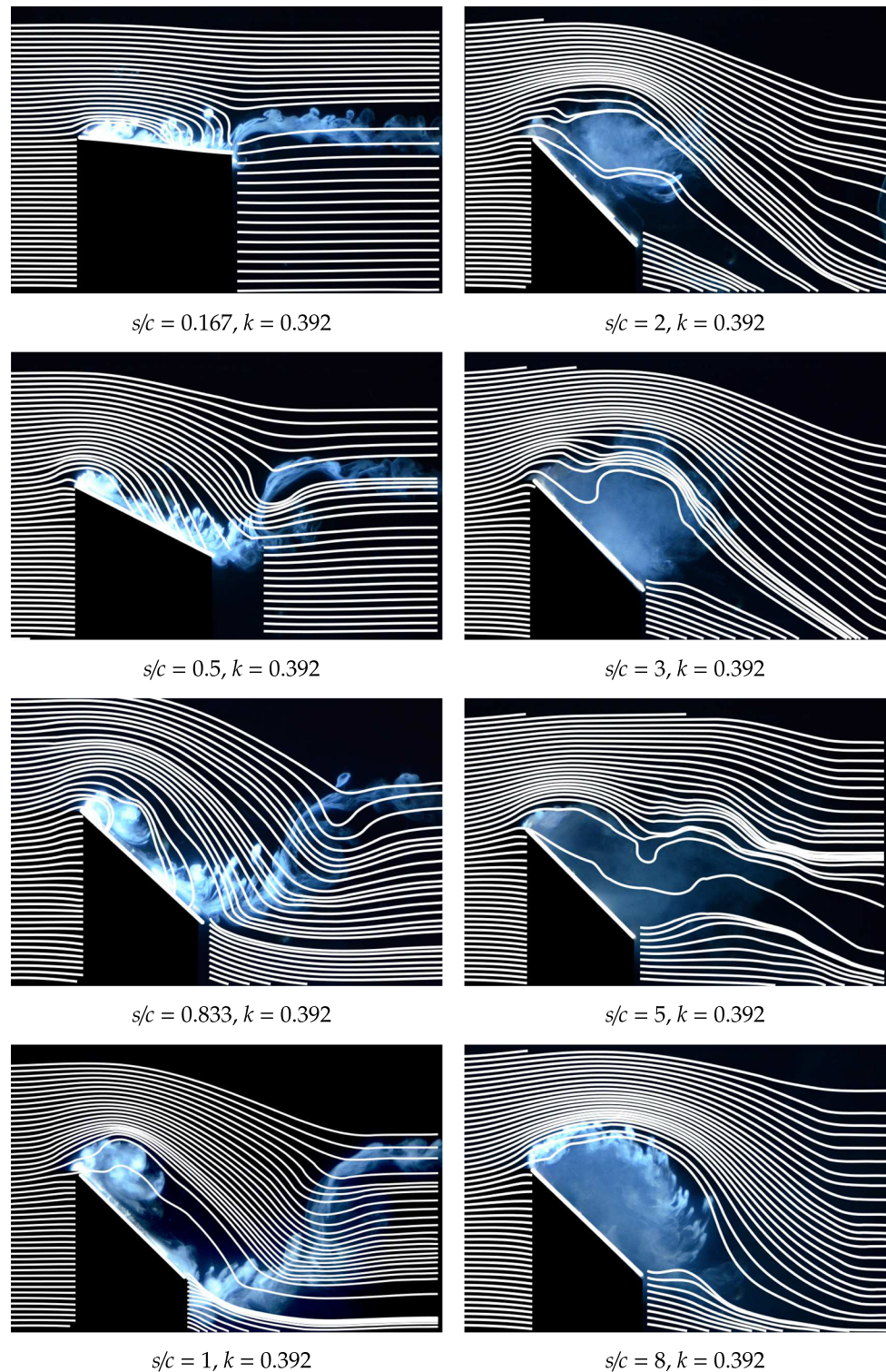
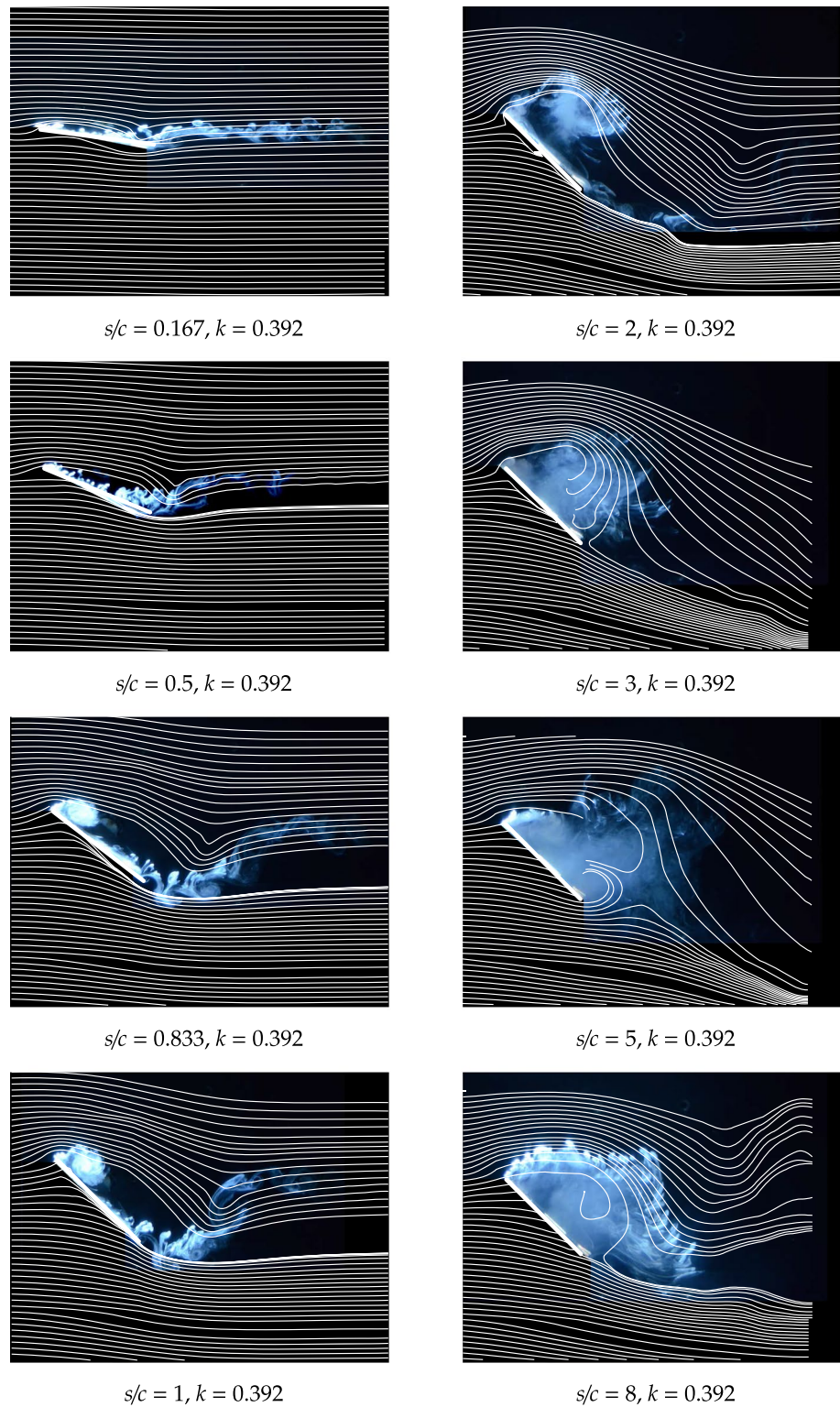


Fig. 15 Dye flow visualisation with streamlines calculated from PIV superimposed (LE pitch)

LEV. In contrast, at the end of pitching ($s/c = 1$), the LEV begins to advect away from the LE. The y -position of the LEV core remains approximately constant until $s/c \approx 1.9$, where it starts to drift upwards.

Multiple TEVs are shed. Each TEV is tracked until the subsequent one forms. A series of 5 TEVs are identified and represented in Fig. 18d. Each TEV has a linear growth in core-relative distance from the TE. The first TEV

Fig. 16 Dye flow visualisation with streamlines calculated from PIV superimposed (Mid pitch)



advects away from the TE in y , as the wing continues to pitch. Thereafter, the TEVs tend to have a downwards drift.

Considering the pitching part of the motion in isolation ($0 < s/c < 1$), the LEV advects at $u_{LEV} \approx 0.1U_{\infty}$ and

TEV_1 at $u_{TEV} \approx 0.7U_{\infty}$. This yields a net relative advection velocity of $0.6U_{\infty}$. The steady state flowfield is complicated by the presence of multiple TEVs but all of them appear to move at approximately the same rate.

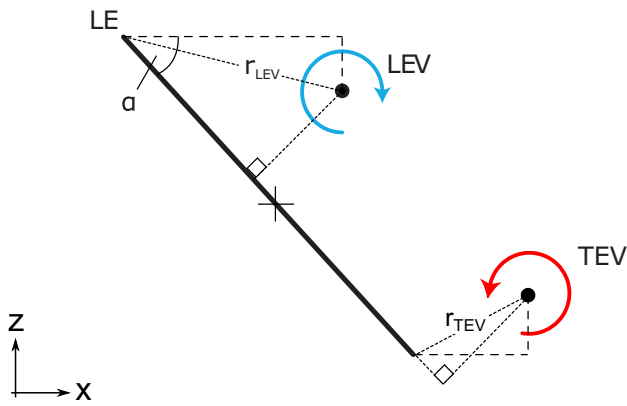


Fig. 17 Leading- and trailing-edge vortex position definition

4.6.3 Effect of pitch axis on vortex dynamics

The relative advection velocities of the first LEV/TEV pair while pitching, for the LE and mid-chord pitch axis, are found to be $0.5U_\infty$ and $0.6U_\infty$, respectively. Given the crude estimate, it is reasonable to state that for both cases

the relative advection velocities are similar. One notable difference between the two axis locations is that for a mid-chord, there are several additional TEVs shed; however, all the TEVs observed have x trajectories that are approximately similar.

4.7 Modified Wagner function

Following a similar reasoning to the aforementioned work by Graham (1983) and the suggestion by Babinsky et al. (2016) that the asymptotic circulation is proportional to the angle of incidence, it is proposed that the Wagner circulation be corrected by the instantaneous incidence factor. This is the instantaneous, effective, incidence angle of the aerofoil, α_{eff} , non-dimensionalised by the maximum (steady translation) incidence angle, α_{max} . The exponential, non-dimensional Wagner circulation is given by the following curve fit function (Babinsky et al. 2016) of:

$$\frac{\Gamma_{LEV}}{\Gamma_\infty} = 0.914 - 0.3151 \exp\left(\frac{s/c}{0.1824}\right) - 0.5986 \exp\left(\frac{s/c}{2.0282}\right) \quad (12)$$

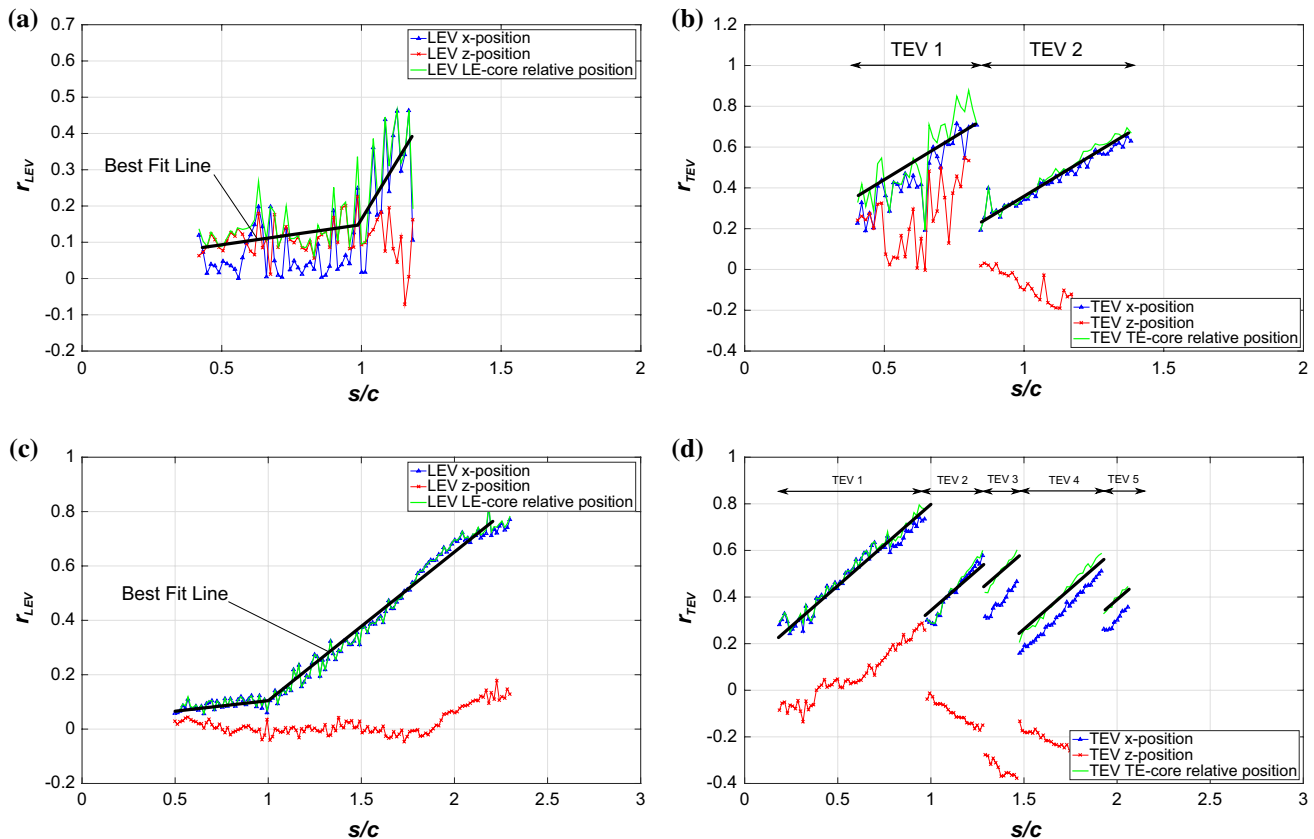


Fig. 18 Fast pitch vortex trajectories at $b/2$, $k = 0.392$, \mathcal{R} , $Re = 10,000$. **a** LEV Trajectory (LE pitch). **b** TEV Trajectories (LE pitch). **c** LEV Trajectory (Mid pitch). **d** TEV Trajectories (Mid pitch)

For a non-dimensional circulation of $\Gamma_{LEV}/\Gamma_\infty$, the corrected theoretical circulation is then given by:

$$\Gamma_p = \frac{\Gamma_{LEV}}{\Gamma_\infty} \cdot \frac{\alpha_{eff}}{\alpha_{max}} \tag{13}$$

where Γ_{LEV} is the vortex (LEV) circulation and Γ_∞ is the circulation equivalent to $C_L = 2\pi \sin\alpha$.

Here the effective angle of incidence ($\alpha_{eff} = \alpha + \alpha_i$) is the sum of the geometric angle of incidence, α and an additional contribution induced by the pitch rotation rate, α_i . Figure 1 defines the pitch axis position relative to the LE, with the induced angle of incidence defined by:

$$\alpha_i = \frac{V \cdot \cos\alpha}{U_\infty} \tag{14}$$

where the plate normal velocity at the mid-chord, V is defined relative to the LE by:

$$V = \left(\frac{c}{2} - x_p\right) \cdot \dot{\alpha} \tag{15}$$

The corrected Wagner curves for a LE and a mid-chord pitch axis, based on a pitch over $s/c = 1$, are compared with the original Wagner approximation in Fig. 19a, b, respectively. Note that in Fig. 19a, there is a small induced incidence at the start of pitching ($s/c = 0$) equivalent to a couple of degrees, but when converted to a circulation increment and then non-dimensionalised, it becomes very small.

4.7.1 LEV Circulation

Figure 20 compares the experimentally determined LEV circulation with the classic Wagner curve and the pitch corrected Wagner curve for both a LE and a mid-chord pitch axis.

For the LE pitch axis case in Fig. 20a, the growth of circulation is quite noisy while pitching, with the circulation approximately following the Wagner exponential but exceeding that predicted by the corrected Wagner curve. After pitching has finished ($s/c = 1$),

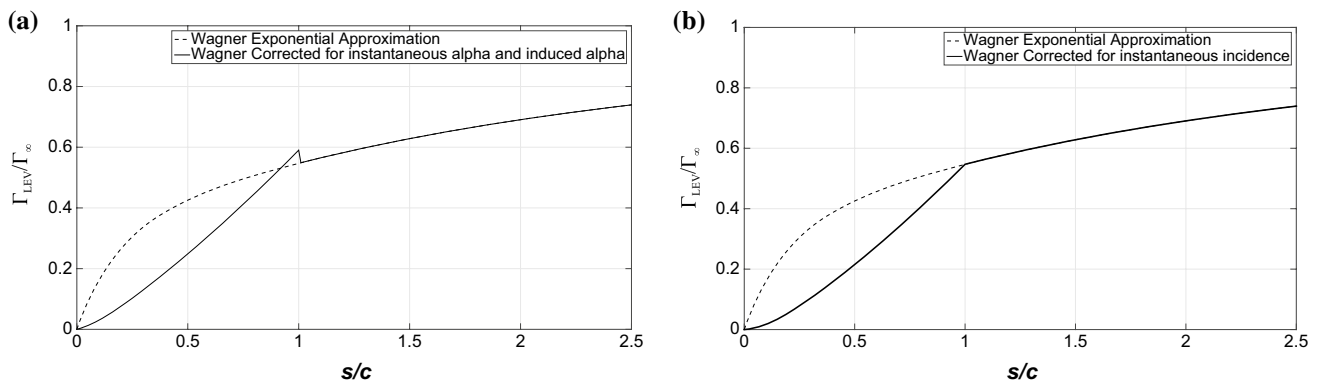


Fig. 19 Corrected Wagner circulation growth (pitch rotation occurs over 1c). **a** LE pitch axis. **b** Mid-chord pitch axis

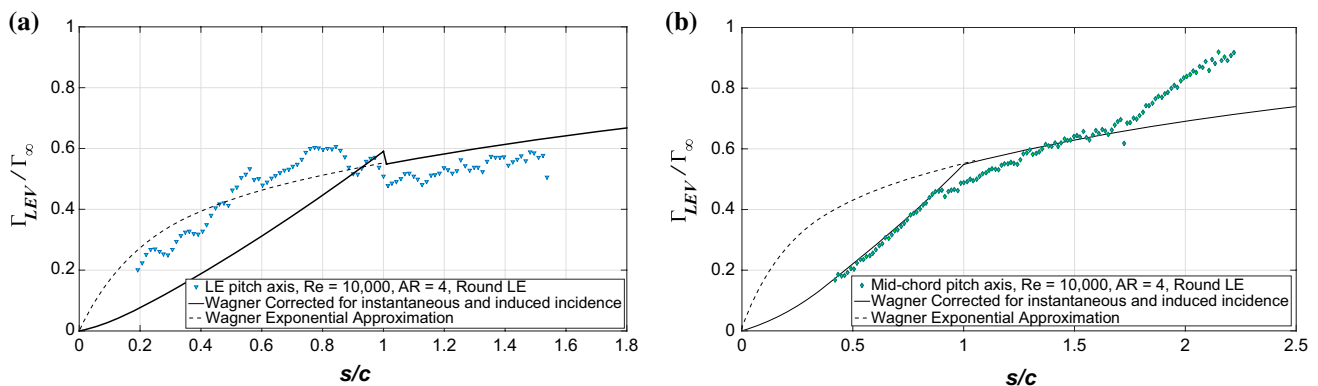


Fig. 20 Experimental (pitch to $\alpha = 45^\circ$, $Re = 10,000$) LEV circulation with Wagner corrected for instantaneous and induced incidence. **a** LE pitch axis. **b** Mid-chord pitch axis

the experimental circulation data is slightly less than the Wagner prediction but with a similar slope. It appears that the unmodified Wagner curve is a better match to the data than the pitch angle corrected version. It is noted that the Wagner prediction is based on a steady state lift coefficient of $2\pi \sin\alpha$. This leads to the surprising suggestion that the LEV circulation grows approximately in the same way as a hypothetical bound vortex on a thin aerofoil operating at 45° , without flow separation. This does not imply that the same level of lift is reached because the LEV does not remain at a fixed position relative to the wing.

For the mid-chord pitch axis case in Fig. 20b, the growth of circulation follows the modified Wagner trend surprisingly well until $s/c \approx 0.9$. By $s/c \approx 1.7$, the experimentally determined circulation diverges from that predicted by Wagner with a much more rapid growth rate, which may possibly be caused by the vortex becoming turbulent as described by Govindaraju and Saffman (1971). Very generally, it can be stated that for a pitch about a mid-chord, the corrected Wagner is a better approximation to the real case than the classic Wagner curve in the region $0 < s/c < 1.75$.

4.8 Reduced-order force model

A comparison between the experimentally measured lift history with that predicted by the reduced-order force model for both the LE and mid-chord pitch axis, respectively, is shown in Fig. 21. Here, the reduced-order model employs the corrected Wagner circulation for both pitch axis cases and uses approximate values for the relative vortex advection velocities as informed by experiment. The experimental data are represented by the broken black curve, with the reduced-order model prediction represented by the green curve. The relative contributions of the contributing terms of the model are also given for reference.

The LE pitch axis of Fig. 21a shows a remarkable correlation between the model prediction and the experimental data, with the general features of the curve being captured well by the model. The model slightly over-predicts the lift force during pitching. The non-circulatory component (broken magenta line) has a large influence on the force during the acceleration and deceleration portion of the pitch rotation. During pitching, the Magnus term and the vortex growth terms are dominant. Initially, at the start of the pitch rotation, the vortex motion term is small but increases through pitching and at the end of pitching is the main contributor to the lift force.

The model again captures the salient features of the measured force history for the mid-chord pitch axis case of Fig. 21b. In contrast to the LE pitch axis case, the mid-chord pitch axis case has no non-circulatory force contribution in accordance with the findings of the ‘wind off’ forces investigation discussed earlier. While pitching the vortex growth and Magnus terms dominate the lift. Similarly to the LE pitch axis case, the vortex motion term is small at the start of pitch rotation but grows and at the end of pitching is the dominant term. The model seems to grossly over-predict the lift force during the pitching motion, and there may be a number of possibly explanations for this. One possibility is that under the presumption that the vortex advection mechanics are similar in both the cases examined then the inclusion of the Magnus term is perhaps questionable. Interestingly, removal of the Magnus term for the mid-chord pitch axis case leads to a much better correlation of the model and the experimental data.

It is emphasised that the model prediction here is based on simplified 2D theory, whereas the lift force measured experimentally is a real, finite wing with tip effects. The ability of the model to capture the shape of the lift history is remarkable; however, a future study might involve a detailed assessment of the sensitivity of the lift force

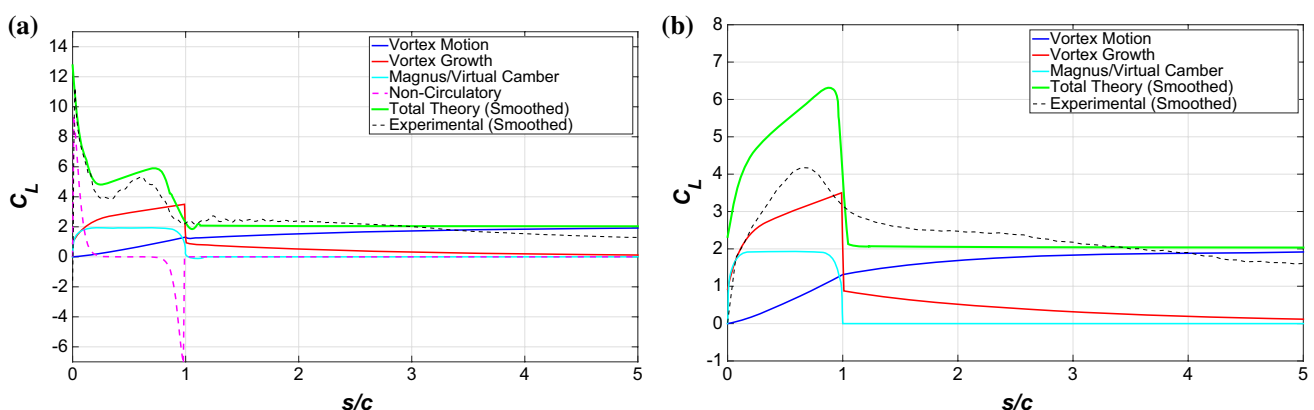


Fig. 21 Comparison of kinematic and vortex dynamics component contributions to lift history with experimental data (Pitch to $\alpha = 45^\circ$, $Re = 10,000$). **a** LE pitch axis. **b** Mid-chord pitch axis

prediction to 3D effects. An evaluation of any sensitivity to such effects could be made by taking PIV and flow visualisation measurements at different plane locations. It is expected, however, that for reasonably high effective AR wings like the one used in this study that the effect of the tip vortex will be confined to the near-tip region. Further studies are also needed to investigate the contributing components which make up the lift force prediction and in particular the Magnus term.

5 Conclusions

An experimental investigation was conducted to study unsteady lift production mechanisms on pitching flat plate wings. The Reynolds number and pitch kinematics were chosen to be representative of the insect/MAV flight regime. A LE pitch and a mid-chord pitch axis were studied.

Analysis of wind off lift forces shows that there is a large non-circulatory spike at the initiation of a pitching rotation for the case of a LE pitch axis, whereas for a mid-chord pitch axis the recorded signal approaches the noise floor.

A twin lightsheet PIV method has proven to be an effective way to provide complete field of view velocity data in a planar sense. Comparing streamlines derived from PIV data with dye flow streaklines gives additional insight. Despite their useful insight when comparing with dye streaklines, streamlines are not Galilean invariant and thus (LEV) vortex cores are obscured since the reference frame moves faster than any vortex induced velocity. In order to calculate the circulation of a LEV from PIV data, a noise-reducing Lamb–Oseen vortex curve fitting technique is used, which is based on an estimated vortex core position.

For a mid-chord pitch axis, there is no observable evidence of any vortical structures below the plate that might have been caused by a vertical shear layer emanating from the LE.

The near-constant advection rate of the LEV while pitching for both a LE and a mid-chord pitch axis indicates that it is ‘attached’, during the pitching motion. It is found that the relative advection velocities of the first LEV/TEV pair for the LE and mid-chord pitch axis move at approximately $0.5U_\infty$ and $0.6U_\infty$, respectively.

It is found that the LEV circulation as calculated from the PIV data approximately matches the general trend of an unmodified Wagner curve for a LE pitch axis and a modified Wagner curve for a mid-chord pitch axis in the pitching phase. The mid-chord pitch axis shows a particularly close correlation with the corrected Wagner curve up until $s/c \approx 1.7$. In both cases, it is assumed that the asymptotic

Wagner circulation is equivalent to that predicted by the *Kutta–Joukowski* theorem for attached flow at 45° . It would be very interesting for a future study to investigate the TEV circulation for each case and see how it compares to the Wagner curves.

Finally, lift forces derived from a 2D reduced-order model have been compared with experimentally measured lift forces. The reduced-order model has circulation and vortex advection velocities informed by experiment. The reduced-order model shows remarkable agreement with experimental data for a LE pitch axis case. For a mid-chord pitch axis case, the lift force is over-predicted during the pitch rotation part of the motion. A logical future study might include investigating the Magnus term further and testing different kinematics. Additionally, future work should include an assessment of the effect of flow three dimensionality and evaluate whether the model needs to be modified to account for the presence of the tip vortex for example.

Open Access This article is distributed under the terms of the Creative Commons Attribution 4.0 International License (<http://creativecommons.org/licenses/by/4.0/>), which permits unrestricted use, distribution, and reproduction in any medium, provided you give appropriate credit to the original author(s) and the source, provide a link to the Creative Commons license, and indicate if changes were made.

References

- Babinsky H, Stevens PRRJ, Jones AR, Bernal LP, OI MV (2016) Low order modelling of lift forces for unsteady pitching and surging wings. In: AIAA SciTech, 54th Aerospace Sciences Meeting, AIAA, San Diego, California, USA, pp 2016–0290
- Beckwith RMH, Babinsky H (2009) Impulsively started flat plate flow. *J Aircr* 46(6):2186–2188
- Brunton SL, Rowley CW (2009) Modeling the unsteady aerodynamic forces on small-scale wings. In: 47th Aerospace Sciences Meeting, AIAA, pp 1127
- Clayton BR, Massey BS (1967) Flow visualisation in water: a review of techniques. *J Sci Instrum* 44(1):2–11
- Davis WR, Kosicki BB, Boroson DM, Kostishack DF (1996) Micro air vehicles for optical surveillance. *Linc Lab J* 9(2):197–214
- Dickinson MH, Götz KG (1993) Unsteady aerodynamic performance of model wings at low Reynolds numbers. *J exp Biol* 174:45–64
- Govindaraju SP, Saffman PG (1971) Flow in a turbulent trailing vortex. *Phys Fluids* 14:2074–2080
- Graftieaux L, Michard M, Grosjean N (2001) Combining PIV, POD and vortex identification algorithms for the study of unsteady turbulent swirling flows. *Meas Sci Technol* 12:1422–1429
- Graham JMR (1983) The lift on an aerofoil in starting flow. *J Fluid Mech* 133:413–425
- Granlund K, OI MV, Garmann DJ, Visbal MR, Bernal L (2010) Experiments and computations on abstractions of perching. In: 28th AIAA Applied Aerodynamics Conference, AIAA, Chicago, vol 2010-4943
- Hartloper C, Kinzel M, Rival DE (2013) On the competition between leading-edge and tip-vortex growth for a pitching plate. *Exp Fluids* 54:1447

- Kang C, Aono H, Baik YS, Bernal LP, Shyy W (2013) Fluid dynamics of pitching and plunging flat plates at intermediate Reynolds numbers. *AIAA J* 51(2):315–329
- Kármán TV, Sears WR (1938) Airfoil theory for non-uniform motion. *J Aeronaut Sci* 5(10):379–390
- Katz J, Plotkin A (2001) *Low speed aerodynamics*. Cambridge University Press, Cambridge
- Lamb H (1932) *Hydrodynamics*, 6th edn. Cambridge University Press, Cambridge
- Leishman JG (2000) *Principles of helicopter aerodynamics*. Cambridge University Press, Cambridge
- Morgan CE, Babinsky H, Harvey JK (2009) Vortex detection methods for use with PIV and CFD data. In: 47th AIAA Aerospace Sciences Meeting, Orlando, Florida
- Nobach H, Bodenschatz E (2009) Limitations of accuracy in PIV due to individual variations of particle image intensities. *Exp Fluids* 47:27–38
- OI MV (2009) The high-frequency, high amplitude pitch problem: airfoils, plates and wings. In: 39th AIAA Fluid Dynamics Conference, AIAA, San Antonio, Texas
- Panah AE, Akkala JM, Buchholz JHJ (2014) Vorticity transport and the leading-edge vortex of a plunging airfoil. *Exp Fluids* 55:1687
- Percin M, van Oudheusden BW (2015) Three-dimensional flow structures and unsteady forces on pitching and surging revolving flat plates. *Exp Fluids* 56:47
- Peters CA (2001) *Environmental Engineering Process Laboratory Manual*, AEEP, Champaign IL, chap Statistics for Analysis of Experimental Data
- Petricca L, Ohlckers P, Grinde C (2011) Micro- and nano-air vehicles: state of the art. *Int J Aerosp Eng* 2011:1–17, Article ID 214549
- PittFord CW (2013) *Unsteady aerodynamic forces on accelerating wings at low reynolds numbers*. PhD thesis, University of Cambridge
- PittFord CW, Babinsky H (2014) Impulsively started flat plate circulation. *AIAA J* 52(8):1800–1802
- Raffel M, Willert CE, Wereley ST, Kompenhans J (2007) *Particle image velocimetry*, 2nd edn. Springer, Berlin
- Theodorsen T (1934) *General theory of aerodynamic instability and the mechanism of flutter*. Tech. Rep. 496, NACA
- Wagner H (1925) Über die Entstehung des dynamischen Auftriebes von Tragflügeln. *Z Angew Math Mech* 5:17–35
- Wang C, Eldredge JD (2012) Low-order phenomenological modeling of leading-edge vortex formation. *Theor Comput Fluid Dyn* 27:577–598
- White FM (2011) *Fluid mechanics*, 7th edn. McGraw Hill, New York
- Young LA, Chen RTN, Aiken EW, Briggs GA (2000) Design opportunities and challenges in the development of vertical lift planetary aerial vehicles. American Helicopter Society International Vertical Lift Aircraft Design Specialist's Meeting, San Francisco CA